Tuning the Optical Absorption of Sn-, Ge-, and Zn-Substituted Cs$_2$AgBiBr$_6$ Double Perovskites: Structural and Electronic Effects

Paz Sebastiá-Luna, Joaquín Calbo, Nicolás Albiach-Sebastián, Michele Sessolo, Francisco Palazón,* Enrique Ortí, and Henk J. Bolink

Read Online

ACCESS | Metrics & More | Article Recommendations | Supporting Information

ABSTRACT: Lead-free halide double perovskites (DPs) are highly tunable materials in terms of chemical composition and optical properties. One of the most widely reported DPs is Cs$_2$AgBiBr$_6$, which is envisaged as a promising absorber for photovoltaics. Nevertheless, its bandgap (around 1.9−2.3 eV) remains too large for common tandem solar cells. In this work, we report the mechanochemical synthesis of Sn-, Ge-, and Zn-substituted Cs$_2$AgBiBr$_6$ in powder form; their bandgaps reach 1.55, 1.80, and 2.02 eV, respectively. These differences are rationalized through density functional theory calculations, demonstrating combined electronic and structural (disorder) effects introduced by the divalent metal-cation substituents. Finally, we present the first vacuum-deposited thin films of the Sn-substituted DP, which also show a notable narrowing of the bandgap, and this paves the way toward its implementation in photovoltaic solar cells.
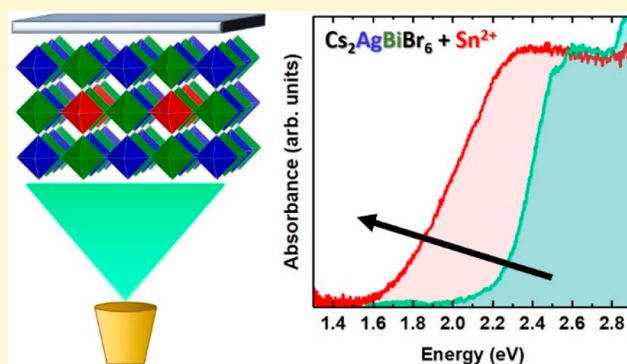
1. INTRODUCTION

Lead halide perovskites (LHPs) have emerged as promising materials for future photovoltaics and other optoelectronic applications. They follow the general formula APbX$_3$, where A is a monovalent cation [Cs$^+$, CH$_3$NH$_3^+$, or CH(NH$_2$)$_2^+$] and X is a halide anion such as Cl$^-$, Br$^-$, or I$^-$. Despite the well-documented performances of lead halide perovskite-based optoelectronics,[1,2] the toxicity of Pb^{2+} ions hinders the widespread application of these materials.[3] By substituting Pb(II) with a combination of B(I) and B(III) cations, while maintaining the same anion framework (see Figure 1), one can readily form double perovskites (DPs).

Halide double perovskites offer a wide range of properties that can compete directly with those of LHPs, such as their longer recombination lifetime at room temperature, higher

heat and moisture stability, and lower toxicity.[4] Their chemical formula A$_2$B$^+$B^{3+}X$_6$, containing one monovalent cation (B$^+$) and one trivalent cation (B^{3+}), shows the large variety of different atomic combinations that can be formed with this stoichiometry. Cs$_2$NaInCl$_6$, Cs$_2$KInCl$_6$, Cs$_2$AgInCl$_6$, Cs$_2$AgSbCl$_6$, and Cs$_2$NaBiCl$_6$ are just a few examples of reported stable DPs.[5] Nevertheless, these chloride DPs typically have bandgap energies of >2.5 eV, which are too large for photovoltaic applications.[6] In this work, we focus on the double perovskite Cs$_2$AgBiBr$_6$, with an indirect bandgap of 1.95 eV, which is closer to a useful value in applications as a wide-bandgap absorber in tandem devices.[4] Indeed, its performance in solar cells has been studied in the literature, but the maximum reported power conversion efficiency (PCE) is only 2.84% with a maximum photocurrent on the order of 5 mA cm^{-2}.[7] It has been suggested that this may be overcome by the use of thicker films to increase absorption.[8] However, Cs$_2$AgBiBr$_6$ films have been reported to have a limited charge diffusion length, which in turn limits the performance of such thicker films as photovoltaic absorbers.[8]
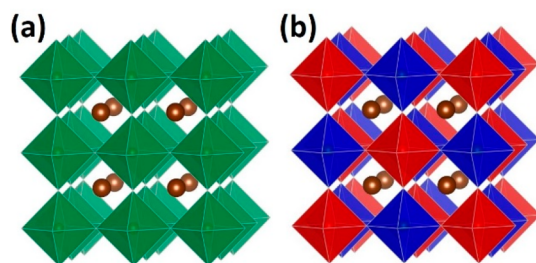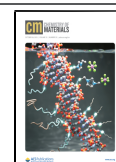

Figure 1. Comparison between the cubic structures of (a) a perovskite AB^{2+}X$_3$ and (b) a double perovskite A$_2$B$^+$B^{3+}X$_6$.

A more efficient absorption of visible light (reduction of the bandgap) is required to ensure future applications of double perovskites in optoelectronics. Partial B-site substitutions have been reported as a strategical route for tackling this issue. Karunadasa and co-workers have demonstrated a bandgap narrowing of ~0.5 eV by using monovalent and divalent cations with the same ns^2 electronic configuration as Bi(III), namely, Tl(I) and Sn(II), altogether with an induced change in the bandgap nature from indirect to direct.[9,10] Nevertheless, the addition of the highly toxic Tl element, the slow solution process synthesis, and the lack of a clear substitution mechanism, could hinder the further development of this B-site substitution. Mitzi and co-workers also found a bandgap decrease of ~0.3 eV by the addition of Sb(III), another element with an ns^2 valence electron configuration.[11] In contrast, addition of In(III), with a different electronic configuration [nd^{10}, same as Ag(I)], was found to increase the bandgap.[11] From these results, a phenomenological rule seems to suggest that ns^2-electronic-configuration substituents (Tl^+, Sn^{2+}, and Sb^{3+}) cause a decrease in the bandgap of $Cs_2AgBiBr_6$, while nd^{10} substituents lead to a bandgap increase. This observation led us to attempt such bandgap tuning through simpler and faster synthetic methods,[12] along with the introduction of new substituents not previously reported experimentally, in particular Ge^{2+} and Zn^{2+}, with ns^2 and nd^{10} electronic configurations, respectively.

Herein, we report the rapid dry mechanochemical synthesis of Sn^{2+}-, Ge^{2+}-, and Zn^{2+}-substituted $Cs_2AgBiBr_6$ and their optical and structural characterization. Note that electronic levels directly introduced by the dopants might not be the only effect at play in tuning the absorption of $Cs_2AgBiBr_6$ (the term dopant is used herein in the general sense of a substituent or an additive, without any *a priori* implication for the concentration of free charges or the position of the Fermi level within the bandgap). Indeed, theoretical studies have shown that the degree of order or disorder in the structure, that is, the precise alternation of $[AgBr_6]^{5-}$ and $[BiBr_6]^{3-}$ octahedra or in contrast the existence of segregated $[AgBr_6]^{5-}$ and $[BiBr_6]^{3-}$ domains, can have a strong influence on the bandgap. In particular, Yang et al.[13] calculated that the bandgap may decrease from 1.93 eV for the fully ordered structure (i.e., perfectly alternating Ag and Bi) to only 0.44 eV for the fully disordered one (i.e., random distribution of Ag and Bi, not fully segregated), with intermediate values closer to those experimentally observed for a partially disordered structure. Furthermore, they showed that the addition of dopants led to a smaller formation energy difference between the ordered and disordered structures. In other words, the lower bandgap observed for doped $Cs_2AgBiBr_6$ could be directly linked to not only electronic effects as previously described, but also to increased structural disorder.

Hence, to rationalize the experimental results obtained with Sn(II), Ge(II), and Zn(II) additives, theoretical calculations are performed in a supercell with a doping ratio of ~15%. Our results confirm a favorable neighboring substitution of the B-site doping cations, resulting in a decrease in the bandgap in going from referable $Cs_2AgBiBr_6$ to Ge^{2+}-doped and Sn^{2+}-doped analogues. The mixing of the frontier occupied and unoccupied B^{2+} dopant orbitals in the valence and conduction bands, respectively, accounts for a change in the electronic dimensionality of the double perovskite, which, together with structural octahedral deformations, leads to an indirect−direct transition of the bandgap.

Finally, Sn-based alloys are processed into thin films by single-source vacuum deposition with different substituent loadings. We demonstrate thus the first DP thin films with increased visible absorption, which paves the way for their implementation in photovoltaics and other thin film-based optoelectronic applications.

2. EXPERIMENTAL SECTION

2.1. Materials. Cesium bromide (CsBr, >99%) was purchased from TCI. Bismuth bromide ($BiBr_3$, ≥98%) and zinc bromide ($ZnBr_2$, 99.999%) were purchased from Sigma-Aldrich. Silver bromide (AgBr, >99.998%) and tin(II) bromide ($SnBr_2$, >99.2%) were purchased from Alfa Aesar. Germanium(II) bromide ($GeBr_2$) was purchased from Biosynth. All chemicals were stored in a nitrogen-filled glovebox and used as received without further purification.

2.2. Mechanochemical Synthesis. An experimental procedure similar to that reported in the literature was followed.[14] Binary precursor salts (CsBr, AgBr, and $BiBr_3$ as well as dopants $SnBr_2$, $GeBr_2$, and $ZnBr_2$) were introduced into 10 mL zirconia ball-mill jars with two zirconia beads that are 10 mm in diameter. Powders were maintained in an inert atmosphere, because the jars were closed inside a nitrogen-filled glovebox. Ball-milling (BM) was performed with a MM-400 shaking ball-mill from Retsch, at a frequency of 30 Hz for 1 and 5 h. Pure DP was synthesized from stoichiometric amounts of CsBr, AgBr, and $BiBr_3$. For the doped samples, calculations were taken considering 1 mol of pure DP as the basis; that is, e.g., for the 15% doped samples, 0.15 mol of the dopant was added to 1 mol of $Cs_2AgBiBr_6$ (molar ratio of 1:0.15).

2.3. Thin Film Deposition by Single-Source Vacuum Deposition (SSVD). In a typical deposition, an alumina thermal crucible (Creaphys GmbH) is placed inside a vacuum chamber and loaded with 350 mg of the as-synthesized $Cs_2AgBiBr_6$ powder (termed "DPp"). Then, the chamber was evacuated to a pressure of 8 × 10^{-6} mbar, and the source is rapidly heated to 550 °C. The deposition is stopped after the complete evaporation of the solid. An average film thickness of 550 nm is deposited, as measured with a mechanical profilometer.

For doped samples, three different starting powders were tested. On one hand, the mechanochemically synthesized 15% $SnBr_2$-doped double perovskite powder was used (DP:15% $SnBr_2$). On the other hand, for the other compositions, an extra amount of dopant is added and hand mixed with the ball-milled double perovskite powder; i.e., 1 mol of the dopant was hand-mixed inside the evaporation crucible with 0.15 (or 1) mol of DP, and the $Cs_2AgBiBr_6$:dopant molar ratio is 1:0.15 (or 1:1). They are termed in the text "DPp+15% $SnBr_2$" or "DPp+100% $SnBr_2$", respectively.

2.4. X-ray Diffraction (XRD) Characterization. X-ray diffraction was measured with a powder diffractometer Empyrean from Panalytical equipped with a Cu Kα anode operated at 45 kV and 40 mA. Single scans were acquired in the $2\theta = 8-60°$ range with a step size of $2\theta = 0.025°$ in Bragg−Brentano geometry in air.

2.5. Optical Characterization. Ultraviolet−visible absorption spectra of the films and powders were recorded using an integrating sphere coupled to an Avantes Avaspec-2048L optical detector (Avantes BV).

2.6. Scanning Electron Microscopy (SEM). SEM images were acquired using a Phenom XL G2Microscope from Thermo Fisher, operating at an acceleration voltage of 10 kV.

2.7. Theoretical Calculations. Theoretical calculations were performed using the density functional theory framework under three-dimensional periodic conditions. The starting crystal structure for double perovskite $Cs_2AgBiBr_6$ was extracted from Materials Project with a cubic crystal system and $Fm\overline{3}m$ space group.[15] Primitive, conventional, and 2 × 2 × 2 lattices were considered in the calculations. In the 2 × 2 × 2 supercell system, subsequent B-site cation substitutions of $^1/_8Ag^+$ and $^1/_8Bi^{3+}$ by $^1/_4Sn^{2+}/Ge^{2+}/Zn^{2+}$ (14% doping concentration) were performed. Minimum-energy crystal structures were obtained by full ion and lattice relaxation at the GGA PBEsol level of theory using a tier 1 numerical atomic orbital (NAO)
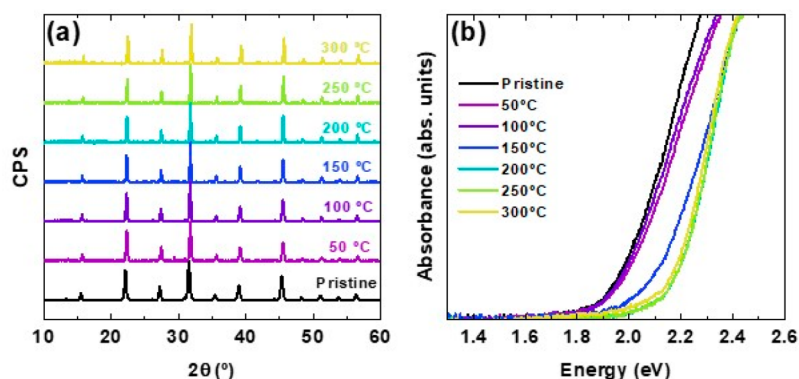
Figure 2. (a) XRD diffractograms of $Cs_2AgBiBr_6$ samples after postsynthesis annealing at different temperatures. (b) Ultraviolet−visible absorption onset to estimate the bandgap.

basis set without applying any symmetry constraints. Defect formation energies (DFEs) for other neutral substitutions with or without the formation of vacancies (V) were calculated: $Sn^{II}_{Ag} + V_{Ag}$, $Sn^{IV}_{Bi} + V_{Ag}$, and $Sn^{IV}_{Ag} + V_{Bi}$. The DFE for neutral defects was obtained according to

$$DFE(X) = E(X) - E(bulk) - \sum_i n_i \mu_i$$

where $E(X)$ is the energy of the defect supercell, $E(bulk)$ is the energy of the pristine supercell, and n and μ are the number and chemical potential, respectively, of the species added ($+$) or subtracted ($-$) from the perfect bulk to form the defect. The sampling k-point grid was set to $6 \times 6 \times 6$, $4 \times 4 \times 4$, and $2 \times 2 \times 2$ for the primitive, conventional, and supercell lattices, respectively. Single-point calculations were further performed at the hybrid HSE06/tier 1 level of theory on the previously GGA PBEsol-optimized crystal structures to obtain the accurate band structures, projected density of states, and bandgap predictions. A general L−Γ−X k-path and k-grids up to $8 \times 8 \times 8$ for primitive, $4 \times 4 \times 4$ for conventional, and $3 \times 3 \times 3$ for supercell lattices were selected to explore the first Brillouin zone of the reciprocal space. Relativistic effects were considered by using the atomic ZORA approximation.[16] Crystal structure and frontier crystal orbital representations were visualized through the VESTA software.[17] All of the calculations were performed by means of the efficient, accurate all-electron, full-potential electronic structure FHI-AIMS code package.[16]

3. RESULTS AND DISCUSSION

Mechanochemical synthesis of $Cs_2AgBiBr_6$ is carried out as described previously.[14] In short, inside a nitrogen-filled glovebox, a stoichiometric amount of CsBr, AgBr, and $BiBr_3$ is introduced inside a 10 mL zirconia ball-mill jar with two zirconia beads that are 10 mm in diameter. The jars are sealed in nitrogen (see the Experimental Section for more details). After being ground for 1 h, the as-synthesized powder is nearly phase-pure $Cs_2AgBiBr_6$ (Figure 2a) with a bandgap of 1.94 eV (Figure 2b). This value is in general agreement with previous literature reports, which present a considerable scattering in values around 1.7−2.3 eV (with most references reporting values in the range of 2.0−2.2 eV).[4,10,11,18−21] This mismatch of bandgap values for the $Cs_2AgBiBr_6$ double perovskite in the literature was previously noticed and studied by Yang and co-workers.[13] Their first-principles calculations point toward the different arrangement of Ag^+ and Bi^{3+} ions as the cause of the bandgap variation. Upon introduction of different levels of cation disorder on the sublattice of Ag−Bi, the band alignment of the whole structure is modified, going from a wider indirect bandgap for the highly ordered structure to a narrower direct

bandgap for the disordered-cation substructure. The ordering of the structure may be tuned by synthetic conditions.[21,22] Herein, the rapid dry ball-milling mechanochemical approach employed is hypothesized to lead to a partially disordered structure, according to the relatively low bandgap value of 1.94 eV with regard to most experimental reports.

When the as-synthesized powders are thermally annealed at different temperatures for 15 min, the absorption edge is found to blue-shift by ≤250 meV (Figure 2b). These results suggest that, as the annealing temperature increases, the double perovskite structure undergoes a conversion from a less ordered structure to a higher-order arrangement of the cations. These changes, which are likely to occur at the atomic scale, cannot be detected by X-ray diffraction within the limits of our instrumentation. In contrast, the similar diffraction pattern for all samples presented in Figure 2a demonstrates the stability of the $Cs_2AgBiBr_6$ DP without any noticeable degradation into other binary or ternary phases.

These results highlight the fact that, without any alloying or doping with extrinsic elements, the bandgap of $Cs_2AgBiBr_6$ can be tuned by synthesis and postsynthesis conditions. Nevertheless, even after a long milling process of 5 h, it appears to be difficult to reach bandgap values below approximately 1.8 eV (see Figure S1). Thus, to obtain narrower bandgap energies, we focused on the incorporation of extra ions into the double perovskite structure. In this case, we incorporated Sn^{2+}, Ge^{2+}, and Zn^{2+} in the mechanochemical synthesis of $Cs_2AgBiBr_6$ and evaluated their effect on the optical absorption of the final compound.

In accordance with previous results with different additives,[9−11] we observe a trend in the bandgap shift according to the electronic configuration of the additive (ns^2 for Sn^{2+} and Ge^{2+} or nd^{10} for Zn^{2+}), in view of the different onset of the ultraviolet−visible (UV−vis) absorption spectra presented in Figure 3. Upon incorporation of small amounts of Sn(II), the absorption of the double perovskite can be significantly red-shifted. Following the previously optimized procedure for the $Cs_2AgBiBr_6$ dry mechanochemical synthesis (see Experimental Section for more details), Sn is incorporated into the double perovskite structure and modifies its optical properties, as one can see by the different colors of the powders (Figure S2). In Figure 3a, the red-shift in the UV−vis absorption is clearly observed, reducing the bandgap from 1.94 eV for the pure DP to 1.55 eV for the highly substituted samples (see Table S1). It is worth mentioning that the bandgap values have been extracted from the Tauc plot,
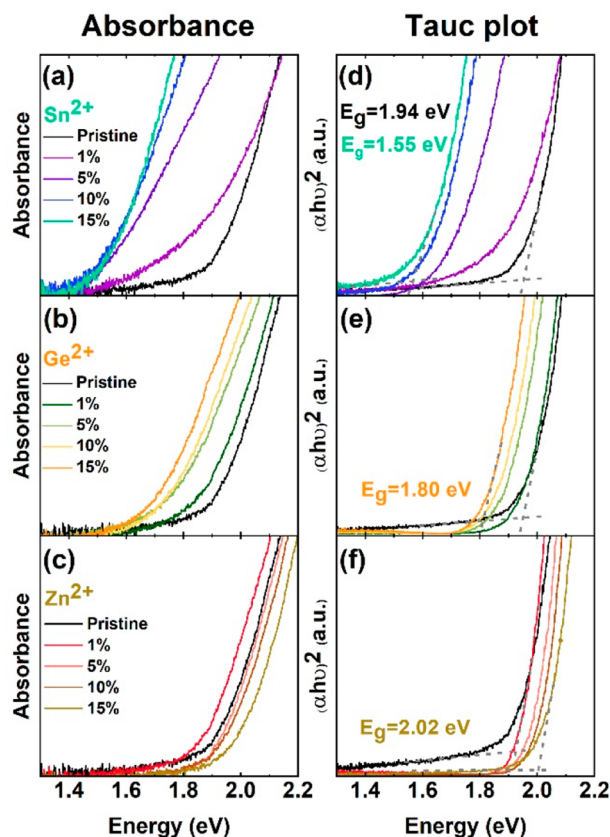
Figure 3. (a−c) Absorbance spectra and (d−f) corresponding Tauc plots of pristine and metal-substituted samples with different loadings as indicated in the legend. Bandgap energies can be estimated by a linear extrapolation of the Tauc plots, as shown in panels d−f. For the sake of simplicity, this extrapolation and estimated bandgap values are only given for the pristine (d) and most substituted samples (d−f), but all values are listed in Tables S1−S3. Tauc plots are derived considering a direct bandgap, which appears to be more accurate than considering an indirect one (Figure S3) and is also supported by theoretical calculations (Figure S11).

because the direct linear extrapolation of the absorbance spectra may be misleading (Figure 3d−f). Frequently, doped materials show sub-band gap absorption states that might have a negative influence in the estimation of the bandgap directly from the UV−vis spectra. In this case, a Tauc plot considering a direct allowed transition has been used to determine the bandgap energies. The choice of a direct transition is based on several reasons. (i) The Tauc plot of pristine $Cs_2AgBiBr_6$ with an indirect transition gives rise to a similar bandgap value compared with that of the direct transition (Figure S3). (ii) For the doped species, the Tauc plot considering an indirect transition does not show the expected linear behavior (Figure S3), which can be considered as experimental evidence of a direct bandgap. (iii) As we will discuss below, theoretical calculations confirm not only the reduction in the bandgap but also the transition from indirect to direct upon doping.

In the same line, the addition of small amounts of Ge(II) also caused a red-shift in the absorption of the double perovskite (Figure 3b). In this case, the bandgap modification is progressive and smoother than for Sn-substituted samples, reaching a bandgap of 1.80 eV (see Figure 3e and Table S2), ideal for the fabrication of tandem solar cells with silicon. This result is also in line with previous calculations in which a large

reduction in the bandgap was predicted by Sn(II) or Ge(II) doping.[23] On the contrary, upon incorporation of $ZnBr_2$, the absorption onset is slightly blue-shifted compared to that of $Cs_2AgBiBr_6$, and the bandgap increases to 2.02 eV for the sample with the highest level of $ZnBr_2$ incorporation (Figure 3c and Table S3).

Notwithstanding the changes in the optical properties, the final structure of the double perovskite is maintained after the incorporation of the additives, without noticeable byproduct phases or particular broadening and/or narrowing of the diffraction peaks in the XRD characterization (Figures S4−S6).
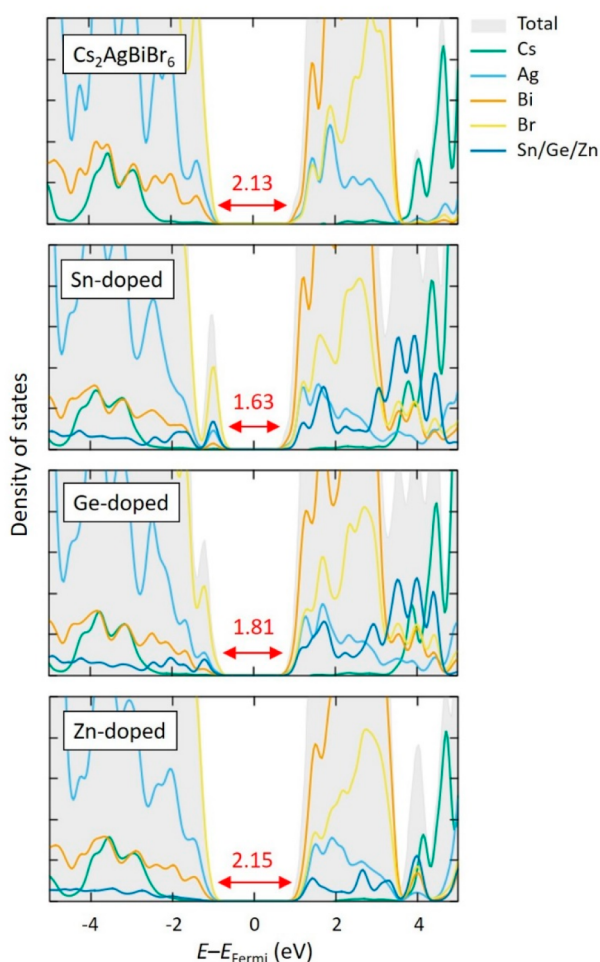
To gain more insight into the structural and electronic effects upon doping, we performed a series of theoretical calculations based on density functional theory. In the primitive unit cell (Figure S8), the reference double perovskite $Cs_2AgBiBr_6$ is predicted with an indirect X−L bandgap of 2.15 eV at the HSE06 level (Figure S9 and Table S4), in relatively good accord with the experimental value of 1.94 eV and with recently reported data.[23] The valence band maximum (VBM) is described mainly by the p orbitals of Br, whereas the conduction band minimum (CBM) is predominantly contributed by the p orbitals of Bi (Figure S10). An extended supercell made by $2 \times 2 \times 2$ primitive unit cells was modeled to assess the effect of B-cation substitution in a 14% ratio (see Experimental Section for details), similar to the highest level of doping experimentally achieved (15%). We considered two doping motifs by substituting either neighboring or distant Ag^+ and Bi^{3+} atoms (Figure 4 and Table S5). Other types of charge-compensating substitutions ($Sn^{II}_{Ag} + V_{Ag}$, $Sn^{IV}_{Bi} + V_{Ag}$, and $Sn^{IV}_{Ag} + V_{Bi}$) were theoretically assessed and found to be higher in energy (Table S6).

Theoretical calculations at the HSE06 level indicate that the "neighboring" substitution is preferred over the "separated"
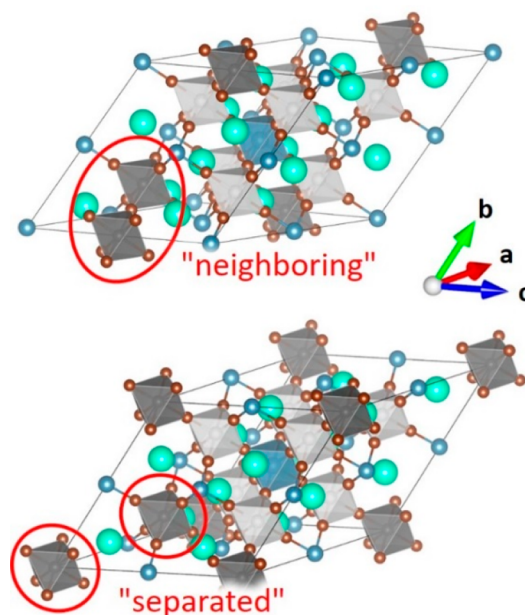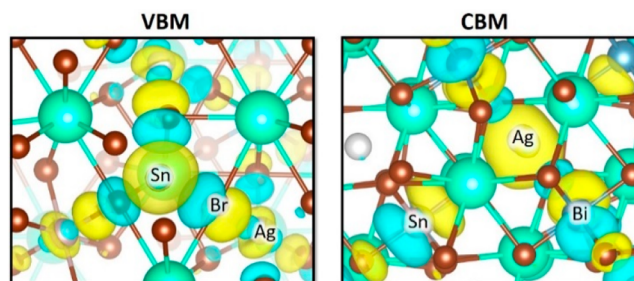

Figure 4. Extended supercells with "neighboring" and "separated" B-cation substitutions in double perovskite $Cs_2Ag_{1-a}Bi_{1-a}X_{2a}Br_6$, where X = Sn, Ge, or Zn and $a = {}^1/_8$. Color coding: light green for Cs, dark blue for Bi (coordination octahedra not shown for the sake of clarity), brown for Br, dark gray for substituted B-cation octahedra, and light gray for Ag-cation octahedra.

disposition, with energy differences of 0.07, 0.18, and 0.51 eV for Sn^{2+}, Ge^{2+}, and Zn^{2+} doping, respectively. These results are in good accord with a recent theoretical study in which the thermodynamic stability of Sn^{2+}/Ge^{2+} B-cation substitution is assessed in the conventional unit cell of $Cs_2AgBiBr_6$.[23] With a focus on the most stable "neighboring" substituted double perovskites, band structure calculations on the supercell show a significant decrease in the bandgap in going from pristine $Cs_2AgBiBr_6$ (2.13 eV) to Ge^{2+}-doped (1.81 eV) and Sn^{2+}-doped (1.63 eV) structures (Figure 5), in very good
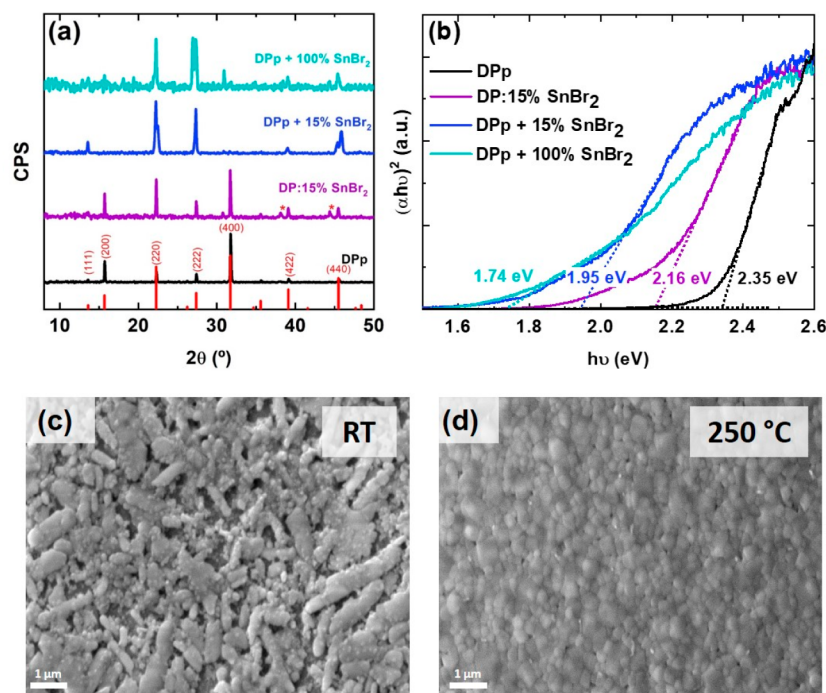

Figure 6. Frontier crystal orbitals corresponding to the VBM and CBM calculated at the HSE06 level for the Sn^{2+}-doped double perovskite. Color coding: light green for Cs, light gray for Ag, blue-gray for Bi, brown for Br, and yellow and turquoise for crystal orbital phases (isovalue of 0.04).

suggestions.[23] Moreover, a significant distortion along with a tilting of the B-site octahedra is predicted upon doping (see Figures S16 and S17). The reduction of the bandgap found experimentally and confirmed theoretically after ns^2 B-site doping therefore implies a significant geometry deformation accompanied by a change in the electronic dimensionality of the double perovskite, rather than a simple inclusion of frontier, discrete defect states by Sn^{2+} or Ge^{2+}.[24]

In contrast to ns^2 doping, nd^{10} Zn^{2+} B-cation substitution leads to a negligible change in the bandgap (2.15 eV) with respect to $Cs_2AgBiBr_6$ (Figure 5). In this case, the relatively deep energy levels of nd^{10} Zn^{2+} do not interact with the VBM, whose nature is described by the Br p and Ag d orbitals (Figure 5), as in the case of the undoped DP. The unoccupied Zn $4s^0$ orbitals are located slightly higher in energy from the CBM and weakly interact with the Bi p and Ag s orbitals (Figure S18). The Zn−Br distances are significantly distorted out of a perfect octahedron (Figure S17); however, this geometry deformation does not introduce frontier defect states within the bandgap.

Considering the experimental and theoretical results reported so far, Sn stands out as the best option to significantly reduce the bandgap of $Cs_2AgBiBr_6$. However, the implementation of these materials in most optoelectronic devices such as solar cells or light-emitting diodes requires their deposition as thin films. Single-source vacuum deposition (SSVD) has been demonstrated to be a fast and reproducible method compatible with a wide range of materials for obtaining thin, smooth, and homogeneous films.[25−28] In this technique, the presynthesized powder materials are placed inside a ceramic crucible in a vacuum chamber. When the crucible is heated at a prefixed temperature under high-vacuum conditions, the materials sublime and deposit on top of a substrate, placed right above the material source. Eventually, thin films with the same composition as the starting materials are deposited onto the substrates.

To the best of our knowledge, SSVD has been employed successfully by others to deposit pure, wide-bandgap, $Cs_2AgBiBr_6$, but it has never been used to prepare thin films of the doped, low-bandgap compositions.[29,30] We first optimized the conditions for the deposition of the undoped DP presynthesized by dry ball-milling (see Experimental Section for further details). As-deposited films do not show the expected diffractogram and optical absorption of $Cs_2AgBiBr_6$ (Figure S19). Similar to what was described in previous reports, we also observed that the as-prepared films presented XRD peaks corresponding to undesirable side phases such as $Cs_3Bi_2Br_9$, with a preferential orientation along the c-

Figure 5. Atom-projected density of states calculated for the supercell of $Cs_2AgBiBr_6$ and its doped analogues at the HSE06 level. The bandgap is indicated in electronvolts.

correlation with the experimental results. Although the major contribution to the VBM (Br-p) and CBM (Bi-p) does not change with respect to the reference $Cs_2AgBiBr_6$, the s and p orbitals of Sn and Ge significantly participate in the frontier bands of the doped material. This can be seen from the density of states (Figure 5 and Figures S12−S14), crystal orbital topologies (Figure 6 and Figure S10), and Mulliken-projected band structures (Figure S11). Importantly, the nature of the bandgap changes from indirect (X−L) to direct (Γ−Γ) upon doping (Figures S9 and S11), which can be explained by the mixing of the s orbital of the doping element (Sn or Ge) with the Br p orbital in the VBM, and of the Sn/Ge p orbital with the Bi p orbital in the CBM (see Figure 6 for the case of Sn^{2+} and Figure S15 for Ge^{2+}), in accord with previous

Figure 7. (a) XRD diffractograms of SSVD thin films of pristine and Sn-doped $Cs_2AgBiBr_6$ samples after annealing at 250 °C. Red asterisks indicate the interfering peaks from the Al platform of the XRD setup. DPp refers to the deposition of pure ball-milled $Cs_2AgBiBr_6$, DP:15% $SnBr_2$ to ball-milled doped $Cs_2AgBiBr_6$:15% $SnBr_2$, DPp+15% $SnBr_2$ to pure ball-milled $Cs_2AgBiBr_6$ with an extra 15% of $SnBr_2$ added and manually mixed in the crucible, and DPp+100% $SnBr_2$ to pure ball-milled $Cs_2AgBiBr_6$ with an extra 100% of $SnBr_2$ added and manually mixed in the crucible. (b) Tauc plots [derived from absorbance spectra (Figure S21)] of post-annealed Sn-doped thin films considering a direct allowed transition. (c) SEM images of pristine DP thin films at room temperature and (d) annealed at 250 °C (scale bar of 1 μm).

axis as one can see by the main peaks at $2\theta = 8.7°$ and $26.3°$ corresponding to the (001) and (003) planes, respectively (Figure S19a).[29,31] This is also in accordance with the observed wide bandgap (Figure S19b). After being annealed at a high temperature (250 °C), these unwanted byproducts vanish to yield the expected $Cs_2AgBiBr_6$ phase (Figure 7a; black diffractogram termed "BM DPp"). This transformation is also linked to important changes in morphology, as observed by SEM (Figure 7c,d). The as-deposited film shows a heterogeneous morphology with anisotropic domains of different sizes. After annealing, the morphology becomes much more homogeneous, with close-packed grains or domains ~500 nm in typical size. High-resolution X-ray photoelectron spectra of Cs 3d, Ag 3d, Bi 4f, and Br 3d signals are presented in Figure S20. Quantitative analysis of the thin film, based on these spectra, yields atomic percentages of 20.3%, 10.4%, 9.2%, and 60.1% for Cs, Ag, Bi, and Br, respectively. This highlights the nearly stoichiometric transfer of the preformed $Cs_2AgBiBr_6$ material by SSVD. Indeed, within instrumental and analysis error, the values are very close to the expected composition. Thin films of the pristine double perovskite present a bandgap of 2.35 eV (Figure 7b), in agreement with previous reports of this material.[32,33]

Finally, we tested the SSVD of Sn-substituted DP. The SSVD of presynthesized 15% Sn-doped powder (DP:15% $SnBr_2$) after annealing at 250 °C led to a slight red-shift of the absorption onset in regard to the pristine composition (Figure 7b and Figure S21). Nevertheless, according to the XRD diffractograms, the overall structure is kept constant, following the same pattern as the annealed pure double perovskite thin films (Figure 7a).

To achieve thin films with a narrower bandgap, more $SnBr_2$ was added to the pure DP inside the evaporation crucible (this is, without previously ball-milling these mixtures), we explored two different ratios (see Experimental Section). When 15% $SnBr_2$ was added to the nondoped DP (DPp+15% $SnBr_2$), there is a further red-shift of the absorption onset of the thin films, achieving a bandgap of 1.95 eV (Figure 7b). Elemental analysis derived from XPS (Figure S22) reveals that in both cases the molar fraction of Sn(II) present in the films is similar and around 5% (independent of whether 15% $SnBr_2$ is added before or after ball-milling). However, the bandgap shift is accompanied by changes in crystallinity (Figure 7a). Indeed, the diffractogram of this sample with $SnBr_2$ added during the evaporation corresponds to the expected $Cs_2AgBiBr_6$ double perovskite phase, albeit with a preferential orientation perpendicular to the (220) and (222) planes (see Figure S23). If the amount of $SnBr_2$ added is increased to a DP:Sn molar ratio of 1:1 (DPp+100% $SnBr_2$), a thin film with a 1.74 eV bandgap was obtained after annealing (Figure 7b) with a crystallinity similar to that of the 15% added film previously discussed (Figure 7a). Elemental and chemical analysis (Figure S22) shows that this drastic addition of 100% in the evaporation crucible leads to an increase in the tin atomic percentage to only 9.5%. Hence, it seems that the process is somehow limited and excess $SnBr_2$ is lost in the evaporation, not incorporated into the crystalline film. It is also worth mentioning that such an important addition of $SnBr_2$ leads to the formation of different Sn species, as evidenced by the secondary, low-binding energy component in the XPS Sn $3d_{5/2}$ spectra (see Figure S22). These results demonstrate that it is possible to obtain homogeneous thin films with the double perovskite crystal structure of $Cs_2AgBiBr_6$ and a tunable

bandgap through the insertion of tin bromide in a fully dry process.

4. CONCLUSIONS

We have studied the bandgap tuning of the $Cs_2AgBiBr_6$ double perovskite synthesized by solvent-free approaches through two different routes: (i) via postsynthesis thermal annealing and (ii) via the introduction of different dopants in the structure. The first method demonstrated that an increase in the annealing temperature leads to a widening of the bandgap, from 1.94 eV for the pristine form to 2.16 eV when annealing at 300 °C. The reason for this phenomenon may reside in the increase in the Ag−Bi lattice ordering upon annealing, which triggers an increase in the bandgap of the double perovskite. In contrast, the incorporation of $SnBr_2$ and $GeBr_2$ into the DP yielded a remarkable red-shift in the absorption onset (1.55 and 1.80 eV, respectively). The addition of $ZnBr_2$, instead, induced a slight increase in the bandgap. The underlying reason for these changes was studied through density functional theory calculations, indicating that Sn^{2+} and Ge^{2+} change the electronic dimensionality of the double perovskite by mixing their occupied s orbitals in the VBM and their unoccupied p orbitals in the CBM. This, in combination with structural octahedral deformations, leads to a significant reduction of the bandgap, in agreement with the experimental results, and to an indirect-to-direct transition in the nature of the gap. Finally, Sn-doped DP thin films were deposited by single-source vacuum deposition. Different dopant concentrations were studied, revealing the possibility of tuning the absorption properties in thin films. These results pave the way to the implementation of cation-substituted $Cs_2AgBiBr_6$ thin films in next-generation optoelectronic devices.

■ ASSOCIATED CONTENT

Ⓢ Supporting Information

The Supporting Information is available free of charge at https://pubs.acs.org/doi/10.1021/acs.chemmater.1c02236.

> XRD diffractograms after annealing; estimated bandgap values for pristine and doped samples; XRD and UV−vis absorption spectra of DP ball-milled for 5 h; pictures of Sn-doped samples; Tauc plots of doped powders considering an indirect bandgap; XRD diffractograms of doped samples; UV−vis absorption spectra of DP doped with Sn^{4+} and Ge^{4+}; theoretical calculations, including representations of unit cells, bandgap values, band structures, density of states, frontier crystal orbital representations, and structural deformation analysis; XPS, XRD, and UV−vis absorption spectra of SSVD pristine and doped DP; and crystal orientation of $Cs_2AgBiBr_6$ (PDF)

■ AUTHOR INFORMATION

Corresponding Author

Francisco Palazón − *Instituto de Ciencia Molecular (ICMol), Universidad de Valencia, 46980 Paterna, Spain;* ⓞ orcid.org/0000-0002-1503-5965; Email: francisco.palazon@uv.es

Authors

Paz Sebastiá-Luna − *Instituto de Ciencia Molecular (ICMol), Universidad de Valencia, 46980 Paterna, Spain;* ⓞ orcid.org/0000-0001-6992-199X

Joaquín Calbo − *Instituto de Ciencia Molecular (ICMol), Universidad de Valencia, 46980 Paterna, Spain;* ⓞ orcid.org/0000-0003-4729-0757

Nicolás Albiach-Sebastián − *Instituto de Ciencia Molecular (ICMol), Universidad de Valencia, 46980 Paterna, Spain*

Michele Sessolo − *Instituto de Ciencia Molecular (ICMol), Universidad de Valencia, 46980 Paterna, Spain;* ⓞ orcid.org/0000-0002-9189-3005

Enrique Ortí − *Instituto de Ciencia Molecular (ICMol), Universidad de Valencia, 46980 Paterna, Spain;* ⓞ orcid.org/0000-0001-9544-8286

Henk J. Bolink − *Instituto de Ciencia Molecular (ICMol), Universidad de Valencia, 46980 Paterna, Spain;* ⓞ orcid.org/0000-0001-9784-6253

Complete contact information is available at: https://pubs.acs.org/10.1021/acs.chemmater.1c02236

Notes

The authors declare no competing financial interest.

■ ACKNOWLEDGMENTS

■ REFERENCES

(1) Jeevaraj, M.; Sudhahar, S.; Kumar, M. K. Evolution of Stability Enhancement in Organo-Metallic Halide Perovskite Photovoltaics: A Review. *Mater. Today Commun.* **2021**, 102159.

(2) Xiang, W.; Liu, S.; Tress, W. A Review on the Stability of Inorganic Metal Halide Perovskites: Challenges and Opportunities for Stable Solar Cells. *Energy Environ. Sci.* **2021**, 2090−2113.

(3) Li, J.; Cao, H. L.; Jiao, W.; Bin; Wang, Q.; Wei, M.; Cantone, I.; Lü, J.; Abate, A. Biological Impact of Lead from Halide Perovskites Reveals the Risk of Introducing a Safe Threshold. *Nat. Commun.* **2020**, *11* (1), 310.

(4) Slavney, A. H.; Hu, T.; Lindenberg, A. M.; Karunadasa, H. I. A Bismuth-Halide Double Perovskite with Long Carrier Recombination Lifetime for Photovoltaic Applications. *J. Am. Chem. Soc.* **2016**, *138* (7), 2138−2141.

(5) Tang, H.; Xu, Y.; Hu, X.; Hu, Q.; Chen, T.; Jiang, W.; Wang, L.; Jiang, W. Lead-Free Halide Double Perovskite Nanocrystals for Light-Emitting Applications: Strategies for Boosting Efficiency and Stability. *Adv. Sci.* **2021**, *8*, 2004118.

(6) Adjogri, S. J.; Meyer, E. L. A Review on Lead-Free Hybrid Halide Perovskites as Light Absorbers for Photovoltaic Applications Based on Their Structural, Optical, and Morphological Properties. *Molecules* **2020**, *25*, 5039.

(7) Yang, X.; Chen, Y.; Liu, P.; Xiang, H.; Wang, W.; Ran, R.; Zhou, W.; Shao, Z. Simultaneous Power Conversion Efficiency and Stability Enhancement of $Cs_2AgBiBr_6$ Lead-Free Inorganic Perovskite Solar Cell through Adopting a Multifunctional Dye Interlayer. *Adv. Funct. Mater.* **2020**, *30* (23), 2001557.

(8) Longo, G.; Mahesh, S.; Buizza, L. R. V; Wright, A. D.; Ramadan, A. J.; Abdi-jalebi, M.; Nayak, P. K.; Herz, L. M.; Snaith, H. J. Understanding the Performance-Limiting Factors of $Cs_2AgBiBr_6$ Double-Perovskite Solar Cells. *ACS Energy Lett.* **2020**, *5*, 2200−2207.

(9) Slavney, A. H.; Leppert, L.; Bartesaghi, D.; Gold-Parker, A.; Toney, M. F.; Savenije, T. J.; Neaton, J. B.; Karunadasa, H. I. Defect-Induced Band-Edge Reconstruction of a Bismuth-Halide Double Perovskite for Visible-Light Absorption. *J. Am. Chem. Soc.* **2017**, *139* (14), 5015−5018.

(10) Lindquist, K. P.; Mack, S. A.; Slavney, A. H.; Leppert, L.; Gold-Parker, A.; Stebbins, J. F.; Salleo, A.; Toney, M. F.; Neaton, J. B.; Karunadasa, H. I. Tuning the Bandgap of $Cs_2AgBiBr_6$ through Dilute Tin Alloying. *Chem. Sci.* **2019**, *10* (45), 10620−10628.

(11) Du, K. Z.; Meng, W.; Wang, X.; Yan, Y.; Mitzi, D. B. Bandgap Engineering of Lead-Free Double Perovskite $Cs_2AgBiBr_6$ through Trivalent Metal Alloying. *Angew. Chem., Int. Ed.* **2017**, *56* (28), 8158−8162.

(12) Palazon, F.; El Ajjouri, Y.; Bolink, H. J. Making by Grinding : Mechanochemistry Boosts the Development of Halide Perovskites and Other Multinary Metal Halides. *Adv. Energy Mater.* **2020**, *10* (13), 1902499.

(13) Yang, J.; Zhang, P.; Wei, S. H. Band Structure Engineering of $Cs_2AgBiBr_6$ Perovskite through Order-Disordered Transition: A First-Principle Study. *J. Phys. Chem. Lett.* **2018**, *9* (1), 31−35.

(14) Rodkey, N.; Kaal, S.; Sebastia-Luna, P.; Birkhölzer, Y. A.; Ledinsky, M.; Palazon, F.; Bolink, H. J.; Morales-Masis, M.; et al. Pulsed Laser Deposition of $Cs_2AgBiBr_6$: From Mechanosynthesized Powders to Dry, Single-Step Deposition. *Chem. Mater.* **2021**, *33*, 7417−7422.

(15) Jain, A.; Ong, S. P.; Hautier, G.; Chen, W.; Richards, W. D.; Dacek, S.; Cholia, S.; Gunter, D.; Skinner, D.; Ceder, G. Commentary: The Materials Project: A Materials Genome Approach to Accelerating Materials Innovation. *APL Mater.* **2013**, *1* (1), 011002.

(16) Blum, V.; Gehrke, R.; Hanke, F.; Havu, P.; Havu, V.; Ren, X.; Reuter, K.; Scheffler, M. Ab Initio Molecular Simulations with Numeric Atom-Centered Orbitals. *Comput. Phys. Commun.* **2009**, *180* (11), 2175−2196.

(17) Momma, K.; Izumi, F. VESTA 3 for Three-Dimensional Visualization of Crystal, Volumetric and Morphology Data. *J. Appl. Crystallogr.* **2011**, *44* (6), 1272−1276.

(18) Smith, M. D.; Connor, B. A.; Karunadasa, H. I. Tuning the Luminescence of Layered Halide Perovskites. *Chem. Rev.* **2019**, *119* (5), 3104−3139.

(19) Jiang, Y.; Li, K.; Wu, X.; Zhu, M.; Zhang, H.; Zhang, K.; Wang, Y.; Loh, K. P.; Shi, Y.; Xu, Q.-H. In Situ Synthesis of Lead-Free Halide Perovskite $Cs_2AgBiBr_6$ Supported on Nitrogen-Doped Carbon for Efficient Hydrogen Evolution in Aqueous HBr Solution. *ACS Appl. Mater. Interfaces* **2021**, *13* (8), 10037−10046.

(20) Ghasemi, M.; Zhang, L.; Yun, J. H.; Hao, M.; He, D.; Chen, P.; Bai, Y.; Lin, T.; Xiao, M.; Du, A.; et al. Dual-Ion-Diffusion Induced Degradation in Lead-Free $Cs_2AgBiBr_6$ Double Perovskite Solar Cells. *Adv. Funct. Mater.* **2020**, *30* (42), 2002342.

(21) Ji, F.; Klarbring, J.; Wang, F.; Ning, W.; Wang, L.; Yin, C.; Figueroa, J. S. M.; Christensen, C. K.; Etter, M.; Ederth, T.; et al. Lead-Free Halide Double Perovskite $Cs_2AgBiBr_6$ with Decreased Band Gap. *Angew. Chem., Int. Ed.* **2020**, *59* (35), 15191−15194.

(22) Kleibeuker, J. E.; Choi, E.-M.; Jones, E. D.; Yu, T.-M.; Sala, B.; MacLaren, B. A.; Kepaptsoglou, D.; Hernandez-Maldonado, D.; Ramasse, Q. M.; Jones, L.; et al. Route to Achieving Perfect B-Site Ordering in Double Perovskite Thin Films. *NPG Asia Mater.* **2017**, *9* (7), e406−e406.

(23) Ma, X.; Li, Z.; Yang, J. Efficient Direct Band Gap Photovoltaic Material Predicted *Via* Doping Double Perovskites $Cs_2 AgBiX_6$ (X = Cl, Br). *J. Phys. Chem. C* **2021**, *125*, 10868−10875.

(24) Xiao, Z.; Meng, W.; Wang, J.; Mitzi, D. B.; Yan, Y. Searching for Promising New Perovskite-Based Photovoltaic Absorbers: The Importance of Electronic Dimensionality. *Mater. Horiz.* **2017**, *4* (2), 206−216.

(25) Sebastia-Luna, P.; Navarro-Alapont, J.; Sessolo, M.; Palazon, F.; Bolink, H. J. Solvent-Free Synthesis and Thin-Film Deposition of Cesium Copper Halides with Bright Blue Photoluminescence. *Chem. Mater.* **2019**, *31* (24), 10205−10210.

(26) El Ajjouri, Y.; Palazon, F.; Sessolo, M.; Bolink, H. J. Single-Source Vacuum Deposition of Mechanosynthesized Inorganic Halide Perovskites. *Chem. Mater.* **2018**, *30*, 7423−7427.

(27) Crane, M. J.; Kroupa, D. M.; Roh, J. Y.; Anderson, R. T.; Smith, M. D.; Gamelin, D. R. Single-Source Vapor Deposition of Quantum-Cutting Yb^{3+}:$CsPb(Cl_{1-x}Br_x)_3$ and Other Complex Metal-Halide Perovskites. *ACS Appl. Energy Mater.* **2019**, *2* (6), 4560−4565.

(28) Longo, G.; Gil-Escrig, L.; Degen, M. J.; Sessolo, M.; Bolink, H. J. Perovskite Solar Cells Prepared by Flash Evaporation. *Chem. Commun.* **2015**, *51* (34), 7376−7378.

(29) Fan, P.; Peng, H.-X.; Zheng, Z.-H.; Chen, Z.-H.; Tan, S.-J.; Chen, X.-Y.; Luo, Y.-D.; Su, Z.-H.; Luo, J.-T.; Liang, G.-X. Single-Source Vapor-Deposited $Cs_2AgBiBr_6$ Thin Films for Lead-Free Perovskite Solar Cells. *Nanomaterials* **2019**, *9* (12), 1760.

(30) Pantaler, M.; Fettkenhauer, C.; Nguyen, H. L.; Anusca, I.; Lupascu, D. C. Deposition Routes of $Cs_2AgBiBr_6$ Double Perovskites for Photovoltaic Applications. *MRS Adv.* **2018**, *3* (32), 1819−1823.

(31) Yang, B.; Chen, J.; Hong, F.; Mao, X.; Zheng, K.; Yang, S.; Li, Y.; Pullerits, T.; Deng, W.; Han, K. Lead-Free, Air-Stable All-Inorganic Cesium Bismuth Halide Perovskite Nanocrystals. *Angew. Chem., Int. Ed.* **2017**, *56* (41), 12471−12475.

(32) Steele, J. A.; Puech, P.; Keshavarz, M.; Yang, R.; Banerjee, S.; Debroye, E.; Kim, C. W.; Yuan, H.; Heo, N. H.; Vanacken, J.; et al. Giant Electron-Phonon Coupling and Deep Conduction Band Resonance in Metal Halide Double Perovskite. *ACS Nano* **2018**, *12* (8), 8081−8090.

(33) Pantaler, M.; Cho, K. T.; Queloz, V. I. E.; García Benito, I.; Fettkenhauer, C.; Anusca, I.; Nazeeruddin, M. K.; Lupascu, D. C.; Grancini, G. Hysteresis-Free Lead-Free Double-Perovskite Solar Cells by Interface Engineering. *ACS Energy Lett.* **2018**, *3* (8), 1781−1786.